Published in Heat Mass Transfer Volume 47, Issue 8, pp.911-919

Modeling Air Entrainment and Transport in a Hydraulic Jump using Two-Fluid RANS and DES Turbulence Models

Dedicated to Prof. Dr.-Ing. Dr.-Ing. E.h. mult. Franz Mayinger on the occasion of his 80th birthday

Jingsen Ma · Assad A. Oberai · Richard T. Lahey, Jr · Donald A. Drew

Abstract Both RaNS (Reynolds-averaged Navier-Stokes) and DES (Detached Eddy Simulation) type turbulence models were used in conjunction with a two-fluid model of bubbly flow and a new subgrid air entrainment model to predict air entrainment and transport in a hydraulic jump. It was found that the void fraction profiles predicted by both methods are in agreement with the experimental data in the lower shear layer region, which contains the air bubbles entrained at the so-called toe of the hydraulic jump. In contrast, in the upper roller region behind the toe, the averaged results of the DES turbulence model gives accurate predictions while a RaNS turbulence model does not. This is because the DES turbulence model successfully captures the strong fluctuations on the free surface which allows it to entrain air near the top of the roller region. In contrast, RaNS type turbulence model results in a steady, smooth interface which fails to capture the wave-induced bubble sources in that region. To our knowledge, this study is the first successful quantitative numerical simulation of the overall void fraction profiles in a hydraulic jump.

Keywords Air Entrainment · DES · RaNS · Hydraulic Jump · Void Fraction · Bubbly Flows

1 Introduction

A hydraulic jump may occur when a stratified liquid flow transitions from being supercritical to subcritical. During this transition, the free surface rises sharply, large-scale turbulence is observed, gas (normally air) is entrained and significant kinetic energy is dissipated. Moreover, significant air/water mass transfer may occur in hydraulic jumps. Because of these characteristics, hydraulic jumps have been widely used by industry for energy dissipation in hydraulic devices, mixing in liquid treatment processes, flow aeration, and they are often observed in rivers and downstream of spillways from dams. Also, similar phenomena are often seen behind the stern of Naval surface ships.

Center for Multiphase Research.
Rensselaer Polytechnic Institute.
110 8th St. Troy, New York 12180-3590. USA.
Tel.:1-518-276-3386 Fax: +1-518-276-4886
E-mail: jingsen.ma@gmail.com · oberaa@rpi.edu ·laheyr@rpi.edu · drewd@rpi.edu

Due to their importance, hydraulic jumps have been extensively studied for centuries, although earlier studies were limited to the liquid phase. One of the earliest investigations of the air entrainment process in a hydraulic jump is the study of Kalinske & Robertson [1], which focused on the total quantity of entrained air. A seminal study was the work of Rajaratnam [2], who made detailed two-phase flow measurements (including the void fraction profiles) in hydraulic jumps for different Froude numbers. Subsequently, numerous experimental studies were carried out on the two-phase aspects of hydraulic jumps. Some good examples are the work of [3–7].

Most prior numerical simulations of hydraulic jumps [8,9,10] have been confined to the liquid phase and have ignored the effect of the entrained air. One of the main difficulties in the two-phase simulation of a hydraulic jump has been the lack of a comprehensive and accurate subgrid air entrainment model. A subgrid air entrainment model is critical for quantitative two-phase flow simulations since a direct numerical simulation (DNS) of this kind of problem, where the entrainment process at the interface is explicitly resolved, is prohibitively costly [11, 12]. Two notable exceptions that account for the multiphase nature of a hydraulic jump are [13] and [14]. In both these studies a subgrid air entrainment model suggested by the former author [13] was utilized to simulate the air ingestion process. However, both of these studies provide only qualitative predictions of two-phase fluid field properties and do not contain quantitative comparisons of void fraction profiles with experimental data.

Recently, a new subgrid air entrainment model was proposed [11, 12]. The basic physics behind this phenomenological model is that air entrainment only occurs when the air cavities just below the interface are drawn into the liquid at a rate that is faster than the downward motion of the local air/liquid interface. In this model the entrained air flow rate is determined by the product of the liquid turbulent kinetic energy and the normal component of the liquid velocity gradient tensor, where the normal direction is pointed into the liquid phase. This subgrid model depends on the physical properties of the liquid and gas and it has been found to successfully predict both the air entrainment location and rate for various types of flows [11, 12], including a plunging liquid jet and the bubbly flow around a Naval surface ship. In each case, this model was evaluated using a Reynolds-averaged Navier-Stokes (RaNS) type turbulent two-fluid model, and the results were assessed by comparisons with experimental void fraction data, and good agreement was found in all cases. However, when the same model was used to simulate a hydraulic jump [11, 12], the simulation only reproduced the void fraction content in the lower turbulent shear layer region but not in the upper roller region (see Fig. 1). This discrepancy was not due to a failure of the air entrainment model, but rather was a natural shortcoming of RaNS-type turbulent two-fluid simulations which do not reproduce the observed strong fluctuations and wave action at the free surface near the top of the hydraulic jump (i.e., in the upper part of the so-called roller region). As a result the entrainment model fails to capture the bubble sources in this region.

In this paper we analyze a hydraulic jump using the subgrid air entrainment model in conjunction with a 3-D two-fluid model of bubbly flow and both a RaNS type and a Detached Eddy Simulation (DES) turbulence model. By comparing these results with experimental measurements we verify that the averaged results of the DES predict the observed void fraction profiles in both the lower shear layer and the upper roller region while, as noted previously, a RaNS type turbulence model misses the latter. To the best of our knowledge this work represents the first accurate, quantitative numerical prediction of the overall void fraction distributions in a hydraulic jump.

In the next Section (Section 2) we describe the RaNS and DES two-fluid turbulence models and the sub-grid air entrainment model that were used in this study. In Section 3, we present the results of the simulations and compare the predicted void fraction profiles with experimental data. Finally, the salient conclusions from this study are given in Section 4.

2 Two-Fluid Model with Air Entrainment

A two-fluid model of bubbly two-phase flow necessarily contains the various conservation equations and the interfacial/wall transfer closure laws for the dispersed gas phase (i.e., the bubbles) and the liquid. Each group of dispersed bubbles within a certain size range is treated as a continuous fluid with ensemble-averaged properties associated with the bubble populations. Both phases have their own separate mass and momentum conservation equations, and for adiabatic flows the phase energy conservation equations are not required.

In this section we introduce the framework of this two-fluid model and the associated subgrid air entrainment model. For simplicity, we have restricted our simulations to one-way coupling where the effect of the dispersed phase (bubbles) on the continuous phase (liquid) is neglected. We model the fluid as composed of a continuous liquid phase and a dispersed gas phase comprised of bubbles of various diameters, which were taken from those measured in the experiments. Readers interested in the effects of two-way coupling are referred to the work of Moraga et al. [15].

2.1 Mass conservation of the bubble phase

The conservation equation of the bubble number density, N_g''', for bubbles of characteristic diameter, D_g, moving with a velocity of u_g, is often referred to as a Boltzmann-type population balance equation [16, 17]. It is given by:

$$\frac{\partial N_g'''}{\partial t} + \nabla \cdot \left(u_g \, N_g''' \right) = \mathcal{E}_g \qquad (1)$$

Where, as discussed below, $\mathcal{E}_g$ is the rate at which the bubble density increases due to air ingestion. Note that other sources of entrained bubbles (e.g., those due to breakup and coalescence) on the right hand side of Eq. (1) were not considered in this study for simplicity, but may be easily included in future work.

The entrained air flux is given by [11, 12]:

$$q(x) = \frac{C_{ent}}{g} k(x) \frac{\partial u_n}{\partial n}(x), \qquad (2)$$

where x is a location vector near the free surface, q is the volume of air entrained per unit interface area, per unit time, C_{ent} is a model coefficient, g is the acceleration due to gravity, k is the local turbulent kinetic energy of the liquid and $\frac{\partial u_n}{\partial n}$ is the normal derivative of the normal component of the liquid velocity at the interface. This model gives the entrained air flux as a volumetric flow rate per unit interfacial area, however, in a two-fluid model the entrained air is normally distributed as a volume source at the interface in a layer that is ϕ_{ent} thick. So the rate of air entrainment per unit volume, per unit time, is:

$$Q(x) = \frac{q(x)}{\phi_{ent}} = \frac{C_{ent}}{g \phi_{ent}} k(x) \frac{\partial u_n}{\partial n}(x), \qquad (3)$$

Finally this volume of air is distributed among bubble groups of different diameters. Thus the change of the number density of bubbles of a given diameter, D_g, per unit volume, per unit time, is given by:

$$\mathcal{E}_g(x) = \frac{C_{ent}}{\phi_{ent} g} \frac{f_E \Delta D_g}{V_{avg}} k(x) \frac{\partial u_n}{\partial n}(x), \qquad (4)$$

where $f_E(D_g)$ is the pdf of the source distribution as a function of the bubble diameter, D_g, which is defined by a user based on related experimental data or empirical laws. In a polydispersed model, ΔD_g is the width of the bubble diameter bin and $V_{avg} = \sum_{D_g} f_E(D_g) v_g \Delta D_g$ is the average bubble volume of a given bin, where $v_g = 1/6 \pi D_g^3$ is the mean volume of a bubble having diameter D_g.

We remark that following [12] the parameter C_{ent} is determined by calibrating the predicted void fraction with experimental results at one point in the domain. The other user-defined parameter ϕ_{ent} is set equal to 2-5 grid lengths close to the air-water interface based on the fact that all the air entrainment takes place

close to the interface.

2.2 Momentum balance of the dispersed phase

The ensemble-averaged balance of momentum equation for the dispersed phase is given by Moraga et al. [18] as:

$$\frac{\partial(v_g N_g''' \rho_d u_g)}{\partial t} + \nabla \cdot (v_g N_g''' \rho_d u_g \otimes u_g)$$

$$= v_g N_g''' \nabla p_c + v_g N''' \rho_d g + M'_g \qquad (5)$$

where ρ_d is density of the dispersed phase, and p_c is the pressure of the continuous liquid phase. Note that M'_g, the fluctuating interfacial force density, must be constituted. This term determines momentum transfer between the continuous phase and the dispersed phase. It may be partitioned into the different types of interactions:

$$M'_g \cong M_g^D + M_g^{TD} + M_g^{VM} + M_g^L + M_g^W \qquad (6)$$

where the right hand side contains contributions due to drag (D), turbulent dispersion (TD), virtual mass (VM), lift (L) and wall-induced forces (W). For the specific expressions for each of theses terms the reader is referred to the work of Moraga et al. [15].

2.3 Conservation laws for the continuous phase

It was assumed that the continuous liquid phase is incompressible and is not affected by the dispersed phase (i.e., one-way coupling). As a result the continuity equation for the liquid phase simplifies to,

$$\nabla \cdot u_c = 0. \qquad (7)$$

The ensemble-averaged statement of the balance of linear momentum for the continuous phase is [15] :

$$\frac{\partial \rho_c u_c}{\partial t} + \nabla \cdot (\rho_c u_c \otimes u_c) s = \nabla \cdot (T_c + T_c^{Re}) + \rho_c g \qquad (8)$$

where $T_c = -p_c I + 2\mu_c D_c$ is the Cauchy stress for a Newtonian fluid, and T_c^{Re} is the Reynolds stress tensor modeled as:

$$T_c^{Re} = -(\frac{2}{3}\rho_c k) I + 2\mu_t D_c, \qquad (9)$$

In the expressions above, I is the identity tensor, μ_c is the continuous liquid's viscosity, D_c is the rate of strain of the liquid phase, and k and μ_t are the turbulent kinetic energy and the liquid's turbulent viscosity, respectively. They are determined by the DES or RaNS turbulence models, which are discussed in Section 2.5.

2.4 Modeling the free surface

The free surface of the air/water mixture was represented using a single-phase level set function ϕ described in [19], which represents the signed distance from the free surface, with the level set, $\phi = 0$, representing the free surface. Its evolution is governed by:

$$\frac{\partial \phi}{\partial t} + u_c \cdot \nabla \phi = 0 \qquad (10)$$

For more details on the application of the single-phase level set method to bubbly flow simulations the reader is referred to the work of Carrica et al. [20] and Moraga et al. [15].

2.5 Turbulence models

For the RaNS simulations, a blended $k-\varepsilon / k-\omega$ turbulence model developed by Menter [21] was used to constitute the Reynolds stress $\mathbf{T}_c^{Re}$. This model employs a blending function so that it behaves like a $k-\omega$ model close to the walls and like a $k-\varepsilon$ model away from walls. A $k-\omega$ model does not require wall-damping functions and uses simple Dirichlet boundary conditions, while a $k-\varepsilon$ model does not exhibit sensitivity to the level of free-stream turbulence as long as the free-stream values are not too high. Thus this blended model combines the relative strengths of both of these turbulence models. Using indicial notation, the balance of turbulent kinetic energy, k, and the turbulent specific dissipation rate, ω, may be expressed as [21, 22]:

$$\frac{\partial k}{\partial t} + \left(u_{cj} - \sigma_k \frac{\partial \nu_t}{\partial x_j} \right) \frac{\partial k}{\partial x_j} - \frac{1}{R_k} \nabla^2 k - \frac{\tau_{ij}}{\rho_c} \frac{\partial u_{ci}}{\partial x_j} + D^k = 0 \qquad (11)$$

$$\frac{\partial \omega}{\partial t} + \left(u_{cj} - \sigma_\omega \frac{\partial \nu_t}{\partial x_j} \right) \frac{\partial \omega}{\partial x_j} - \frac{1}{R_\omega} \nabla^2 \omega - \gamma \frac{\omega}{k} \frac{\tau_{ij}}{\rho_c} \frac{\partial u_{ci}}{\partial x_j}$$

$$+ \beta \omega^2 + 2(1 - F_1) \sigma_{\omega 2} \frac{1}{\omega} \frac{\partial k}{\partial x_j} \frac{\partial \omega}{\partial x_j} = 0 \qquad (12)$$

where $\mathbf{u}_c$ is the liquid velocity, $\mathbf{t}_{ij}$ is the stress tensor and σ_k, σ_ω, β, and γ are model coefficients, which are given elsewhere [21, 22]. In this model F_1 is a blending function, which is designed to be unity in the laminar sublayer and logarithmic regions of boundary layers and gradually switches to zero in the so-called wake region. The process of determining its specific value is given by Menter [21]. Here $R_k = 1/(\frac{\mu_c}{\rho_c} + \sigma_k \nu_t)$ and $R_\omega = 1/(\frac{\mu_c}{\rho_c} + \sigma_\omega \nu_t)$ are defined using the liquid's viscosity, and turbulent kinematic viscosity, ν_t. The dissipative term, D^k, in the liquid kinetic energy transport equation, Eq.(11), is given by Menter [21] as :

$$D^k = \beta^* k\omega, \tag{13}$$

where β^* is a coefficient given by Moraga et al.[15].

A detached eddy simulation (DES) is a hybrid turbulence model which switches from a RaNS turbulence model to a type of Large Eddy Simulation (LES) in regions where the grid resolution is sufficient to resolve the large scale turbulence. This strategy was implemented within the framework of Menter's RaNS turbulence model [21] described above by following the work of Travin et al.[23]. The equations are exactly the same as in the RaNS type turbulence model described above in Eqs. (11) and (12), the only exception being the definition of the dissipative term in the turbulent kinetic energy equation, which is given by:

$$D^k = \frac{k^{3/2}}{\tilde{l}}, \tag{14}$$

where,

$$\tilde{l} = \min\left(\frac{k^{1/2}}{\beta^*\omega}, C_{DES}\Delta\right) \tag{15}$$

In the equation above Δ is a measure of the local grid size. It can be seen that a LES is activated whenever the grid-based length scale is smaller than the turbulent length scale calculated using the $k-\omega$ model, that is ($k^{1/2}/(\beta^*\omega)$). As a result, a LES can be intentionally applied, via an a-priori design of grid resolution, to select regions in the flow. The DES constant in our simulations was set to $C_{DES} = 0.65$, a typical value used for the analysis of homogeneous turbulence [15].

3 Numerical Simulation

Using the above computational multiphase fluid dynamic (CMFD) methodology we have simulated a hydraulic jump with a Froude number of 1.98 using both RaNS and DES turbulence models. We have noted the locations at which the air entrainment model predicts air ingestion. We have also predicted the void fraction distributions at different locations downstream of the toe of the hydraulic jump and compared them with the experimental measurements reported by Murzyn et al. [7].

3.1 **Experimental and simulation setup**

The experimental setup of Murzyn et al. [7] is shown schematically in Figure 1. Water was discharged from beneath a sluice gate into a 0.30m wide, 0.4m deep and 12m long horizontal re-circulating glass-sided channel. The water flow entered at an average velocity of u_j = 1.50 m/s and it experienced a hydraulic jump at a distance of about 0.36 m after the gate, from an upstream depth D_j of 0.059 m, to a downstream depth of about 0.138 m. This transition occurred while the boundary layer at the bottom surface was only partially developed. The flow had a Froude number of F_r =1.98 and a Reynolds number of $Re = 8.85 \times 10^4$, which was calculated based on u_j and D_j. Detailed air/water flow measurements were made at several downstream locations.

In order to control the computational costs associated with simulating this problem, the RaNS simulations were performed in a pseudo two-dimensional domain that was 4 D_j deep and 30 D_j long. As seen in Fig.2, a 181×100 (length × depth) structured mesh with variable size was used. The mesh was finest near the toe region of the hydraulic jump and where the experimental data was available, becoming coarser in both the upstream and downstream directions. Grid convergence was verified by repeating the calculations on a finer mesh with twice the resolution near the toe region, without observing any significant differences. For the DES run, the same domain and grid size as the RaNS calculation were used in the length and depth directions. However the DES grid was three dimensional in order to capture the large scale turbulent structures that are necessarily three-dimensional. In the third direction (width) the domain was set to 5 D_j, which was the width of the experimental channel, and was modeled with 40 cells.

Boundary conditions were specified at the six faces of the computational domain. On the left face of the computational domain, which corresponds to the sluice gate in the experiment, the horizontal component of the liquid velocity was uniformly set to 1.5m/s, and $Fr = 1.97$ and $R_e = 8.85 \times 10^4$ were imposed. All other liquid and gas velocity components and the bubble number density function were set to zero. A zero-gradient boundary condition was selected for pressure, and the level set function was set to the signed distance from the zero level set (i.e., the interface), which was prescribed to be of unit

distance from the bottom surface. The turbulent variables, k and ω, were set to their free-stream values of $9\times10^{-5}/Re$ and 0.09, respectively, where Re is the Reynolds number based on the inflow velocity and depth. These free-stream quantities were determined by following the procedure suggested by Menter [21], to ensure they are small enough to not influence the solution of turbulence. On the right face, a zero gradient boundary condition was used for all variables. On the top face the piezometric pressure was set to zero, and a zero gradient boundary condition was used for all other variables [22,24]. On the bottom face, a no-slip boundary condition was imposed [24, 22]. In addition, zero-gradient conditions were applied to both the front and back vertical walls. For the initial conditions, all velocities, pressure and bubble number density functions were set to zero and, as noted previously, the initial level set function was set to the signed distance from the interface at $y/D_j = 1$.

For the gas (i.e., air) phase, the entrainment depth was set to be ϕ_{ent} = 0.2 D_j for both RaNS and DES runs. The air entrainment model coefficient C_{ent} was taken to be 0.5, and 1.9 for the RaNS and DES runs respectively. In both runs, two groups of bubbles with f_E = 0.5 for each were studied, having diameters of 1mm and 7mm, respectively, approaching a mean diameter of around 4mm, which was the average bubble diameter reported in the experiments of Murzyn et al. [7]. The non-dimensionalized time step was 0.03, which translates to a dimensional time interval of about 1.2×10^{-3} s.

3.2 **Simulation results**

After about 10,000 time steps (i.e., 12s) the RaNS simulation reached a steady-state, characterized by a smooth, steady free surface everywhere (seen in Fig. 3a). The flow experiences a hydraulic jump at a distance of about $6\,D_j$ downstream from the inlet gate, with a partially developed velocity profile underneath the toe of the hydraulic jump. This results in a downstream depth of about $2.2\,D_j$, which is consistent with experimental observations. We continued the RaNS simulation for another 2,000 time steps to verify that all variables remained at steady state and used the results from the final step of the simulation for comparisons with the experimental data. We also projected this final state on to the three-dimensional grid and used it as the initial condition for subsequent DES simulations. In the DES runs, the free surface very quickly developed surface waves, as can be seen in Fig. 3b. We monitored the time-averaged DES properties and noted that statistically-stationary results were obtained after about 10^4 time steps.

In Figure 3a the kernel of the air entrainment source strength in Eq.(4), that is $k\dfrac{\partial u_n}{\partial n}$, is plotted for the RaNS simulation. We observe that there is strong entrainment at the toe of the hydraulic jump, but

nowhere else. A look at the streamlines in Fig. 4 reveals the presence of a large region of recirculation, often referred to as a roller, just downstream of the toe. This feature has been widely observed in experimental studies of hydraulic jumps, and also in prior simulations [13, 14, 11, 12]. We observe that air entrainment occurs when the recirculating liquid stream from the roller impinges on the liquid stream right below the toe. This leads to an increase in the horizontal component of the liquid velocity in the horizontal direction, causing air to be entrained into the hydraulic jump. Next in Fig. 3b we have plotted the air ingestion kernel for the DES run. In this case air entrainment occurs not only at the toe, but also along the free surface of the roller region where significant wave action is observed at each instant. To our knowledge this source of air entrainment has not been captured in prior numerical simulations of hydraulic jumps, even though it has been observed in numerous experimental studies. For example, Misra et al.[25] concluded that in the roller region downstream of the toe, the free surface exhibits large fluctuations that are associated with the entrainment of air cavities or pockets. Rodriguez-Rodriguez et al.[26] also reported that the agitation of the free surface in this region entraps air cavities that are subsequently broken up into smaller bubbles by the surrounding liquid turbulence.

Next we compare the predictions of void fraction with experimental data. In Figure 5, each plot contains experimental and simulated (RaNS and DES) void fraction profiles as a function of the normalized vertical coordinate, where $Y / D_j = 0$ denotes the bottom of the channel. The RaNS results are from the final steady-state, while the DES were temporally and spatially (in the spanwise direction) averaged. Note that during the averaging interval used for the DES runs it is possible that a given point may lie within the two-phase fluid at one instant and in the air at another. That is, it may be below the nominal free surface at one instant and above it at anoother. When a point is below the free surface its void fraction is set to the value predicted by our 3-D two-fluid code, and when it is above the free surface it is set to unity. These results are then time-averaged. This approach of determining the void fraction is consistent with the intrusive measurement technique used in the experiments. While moving from the top to the bottom in Fig. 5, the downstream measurement locations (measured from the toe) were, $X = 0.85D_j$, $1.70D_j$ and $2.54D_j$.

For the RaNS results, we note that the lower half of the void fraction profiles, corresponding to the shear layer region, match the experimental data quite well at all locations. This indicates that our phenomenological air entrainment model accurately predicts the location and the strength of the air entrainment at the toe, which is responsible for the bubbles observed in the shear layer. It also demonstrates that the two-fluid model accurately transports the bubbles once they are entrained at the toe. We note that with increasing downstream distance, X, the void fraction distribution spreads out due to turbulent dispersion and that the peak of the distribution moves upward due to bubble buoyancy, which is consistent with experimental observations. On the other hand, things are very different when we examine the upper half of the profiles, which correspond to the roller region. We observe that the predicted void fraction

obtained from the RaNS simulation decreases with increasing vertical coordinate, until it reaches the interface where it jumps to unity (not shown). Contrary to this, the experimental data indicates that the void fraction increases monotonically from the value at the boundary between the shear layer and the roller regions to unity just above the mean interface.

In contrast to the RaNS results, we observe in Fig. 5 that the DES results match the experimental observations well both in the lower shear layer and in the upper roller region. The air concentration predicted by the DES turbulence model in this roller region is composed of two parts. One contribution is due to the additional bubble sources on the top of the roller captured by the air entrainment model, as shown in Fig. 3b. The other is due to the successful reproduction of the free surface fluctuations at the top of the roller region. The void fraction associated with the averaged wave-action is a significant contributor to the high void fraction observed in this region. Due to the waves on the gas/liquid interface it is likely that a fixed spatial point close the mean interface will be included in a large air cavity, or be completely contained in the gas region for a fraction of time. If so, when computing the void fraction, the air-indicator function would assume a value of unity for these instances. Due to time-averaging, this would, in turn, lead to relatively large void fraction values just below the mean interface. Note that these values are not due to a large concentration of bubbles in this region, but rather due to the transient topology of the interface. In the RaNS simulation this wave structure is not captured while in the DES results it is. As a result the void fraction results predicted by the latter would be expected to better match the experimental measurements, and they do. All of these can be clearly seen by comparing the middle and the right columns in Fig. 5, which tells that the void fraction near the top of the roller region of the hydraulic jump is due more to the averaging of the wavy interface than the air entrained by the entrainment model.

4 Conclusions

Using a phenomenological subgrid air entrainment model [11, 12] and a turbulent two-fluid model, two-phase CMFD simulations of a hydraulic jump at a Froude number of 1.98 were carried out using both RaNS and DES turbulence models. The predicted results for the void fraction profiles were compared with experimental data. It was observed that while both the RaNS and DES simulations correctly predict the air entrainment at the toe of the hydraulic jump, only the DES model reproduces the air entrainment at the wavy free surface on top of the roller region. This is because the RaNS simulation results in a completely smooth, steady free surface, while the DES turbulence model predicts a turbulent rough/wavy structure similar to what is observed in experiments. As a result, the RaNS simulations accurately predict the void fraction profile only in the lower turbulent shear layer region, while the DES model does a good job in both the lower turbulent shear layer and the upper roller regions.

The results of this study also point to interesting and important differences between the RaNS and DES type turbulence models and indicate that one should choose the appropriate model to meet the objectives of a particular two-phase flow simulation. RaNS simulations incur smaller computational costs and might be sufficient when the region of interest is quite distant from gas/liquid interfaces, for example, in plunging liquid jets or the effect of the air entrainment due to bow waves around a moving Naval surface ship. A DES turbulence model, on the other hand, is computationally more expensive, but it has the ability to provide more accurate multiphase results closer to highly agitated gas/liquid interfaces. Thus, for example, it may be the appropriate modeling approach to use when studying the influence of entrained bubbles on optical scattering in the upper ocean due to breaking sea waves or for the wake behind Naval surface ships.

Acknowledgements This work was supported by the Office of Naval Research (ONR), Grant N00014-03-1-0826, under the administration of Dr. Patrick Purtell, and was also supported in part by a generous grants of computer time from the DOD High Performance Computing Modernization Program at the Maui High Performance Computing Center (MHPCC), US Army Engineering and Research Development Center (ERDC) and Arctic Region Supercomputing Center (ARSC). We also thank Dr. Frederic Murzyn at Parc Universitaire de Laval-Change for providing us with his detailed experimental data on void fractions in hydraulic jumps.

References

[1] Kalinske, A., Robertson, J. (1943) Closed conduit flow. Transactions, ASCE **108**:1435--1447

[2] Rajaratnam, N. (1962) An experimental study of air entrainment characteristics of the hydraulic jump. J. Inst. Engng India **42**(7):247 -- 273

[3] Resch, F., Leutheusser, H. (1972) Le ressaut hydraulique : mesure de turbulence dans la rgion diphasique. Jl La Houille Blanche **4**: 279--293

[4] Chanson, H. (1996) Air Bubble Entrainment in Free-Surface Turbulent Shear Flows. Academic Press

[5] Mossa, M., Tolve, U. (1998) Flow visualization in bubbly two-phase hydraulic jump. Journal of Fluids Engineering **120**(1):160--165

[6] Chanson, H., Brattberg, T. (2000) Experimental study of the air-water shear flow in a hydraulic jump. International Journal of Multiphase Flow **26**(4):583 -- 607 .

[7] Murzyn, F., Mouaze, D., Chaplin, J. (2005) Optical fibre probe measurements of bubbly flow in hydraulic jumps. International Journal of Multiphase Flow **31**(1):141 -- 154 .

[8] Liu, Q., Uwe, D. (1994) Turbulence characteristics in free and forced hydraulic jumps. Journal of hydraulic research **32**:877--898

[9] Stelling, G.S., Busnelli, M.M. (2001) Numerical simulation of the vertical structure of discontinuous flows. International Journal for Numerical Methods in Fluids **37**(1): 23--43.

[10] Zhou, J., Stansby, P. (1999) 2d shallow water flow model for the hydraulic jump. International Journal for Numerical Methods in Fluids **29**(4): 375--387

[11] Ma, J., Oberai, A., Drew, D., Lahey Jr, R., Hyman, M. (2009) A comprehensive subgrid air entrainment model for Reynolds-averaged simulations of free-surface bubbly flows. In: APS DFD Meeting Abstracts

[12] Ma, J., Oberai, A., Drew, D., Lahey Jr, R., Hyman, M. (2011) A comprehensive sub-grid air entrainment model for RaNS modeling of bubbly flows near the free surface. The Journal of Computational Multiphase Flows **3**(1): 41 -- 56

[13] Souders, D.T., Hirt, C.W. (2004) Modeling entrainment of air at turbulent free surfaces. In: Proceedings of World Water and Environmental Resources Congress 2004

[14] Gonzlez, A.E., Bombardelli, F.A. (2005) Two-phase-flow theoretical and numerical models for hydraulic jumps, including air entrainment. In: Proc. XXXI IAHR Congress

[15] Moraga, F.J., Carrica, P.M., Drew, D.A., Lahey Jr., R.T. (2008) A sub-grid air entrainment model for breaking bow waves and naval surface ships. Computers & Fluids **37**(3):281 -- 298.

[16] Martinez-Bazan, C., Montañes, J., Lasheras, J.C. (1999) On the breakup of an air bubble injected into a fully developed turbulent flow. Part 1. Breakup frequency. J. Fluid Mech. **401**:157--182

[17] Larreteguy, A.E., Drew, D.A., Lahey Jr., R.T. (2002) A center-averaged two-fluid model for wall-bounded bubbly flows. In: Proc. 2002 Joint US ASME/European Fluids Engineering Division Summer Meeting. Montreal. Canada

[18] Moraga, F.J., Larreteguy, A.E., Drew, D.A., Lahey Jr., R.T. (2006) A center-averaged two-fluid model for wall-bounded bubbly flows. Computers & Fluids **35**:429--461

[19] Sussman, M., Smereka, P., Osher, S. (1994) A level set approach for computing solutions to incompressible two-phase flow. Journal of computational Physics **114**(1):146--159

[20] Carrica, P., Wilson, R., Stern, F. (2006) An unsteady single-phase level set method for viscous free surface flows. International Journal for Numerical Methods in Fluids **53**(2): 229--256

[21] Menter, F.R. (1994) Two-equation eddy viscosity turbulence models for engineering applications. AIAA Journal **32**(8):1598--1605

[22] Paterson, E.G., Wilson, R.V., Stern, F. (2003) General-purpose parallel unsteady rans ship hydrodynamics code: Cfdship-iowa. IIHR Report 432, Iowa Institute for Hydraulic Research. The University of Iowa, Iowa, USA.

[23] Travin, A., Shur, M., Strelets, M., Spalart, P.R. (2002) Physical and Numerical Upgrades in the Detached-Eddy Simulation of Complex Turbulent Flows, pp. 239--254. Springer Netherlands

[24] Moraga, F.J., Larreteguy, A.E., Carrica, P.M., Drew, D.A., Lahey Jr., R.T. (2001) CFDShipM: Multiphase Code for Ship Hydrodynamics. Version 3.02.02 Users manual.

[25] Misra, S.K., Brocchini, M., Kirby, J.T. (2006) Turbulent interfacial boundary conditions for spilling breakers. In: Proceedings of the 30th International Conference of Coastal Engineering

[26] Rodriguez-Rodriguez, J., Marugan-Cruz, C., Aliseda, A., Lasheras, J.C. (2011) Dynamics of large turbulent structures in a steady breaker. Experimental Thermal and Fluid Science **35:** 301–310

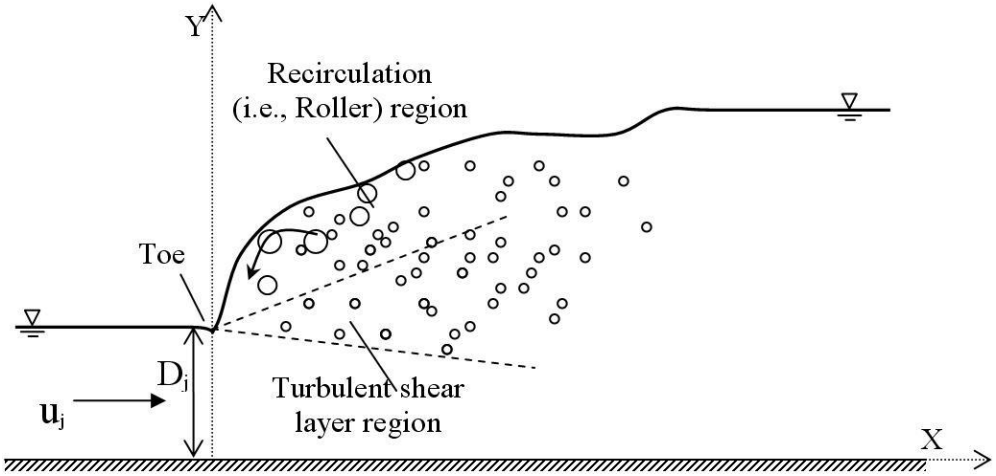

Fig. 1 Schematic diagram of the hydraulic jump.

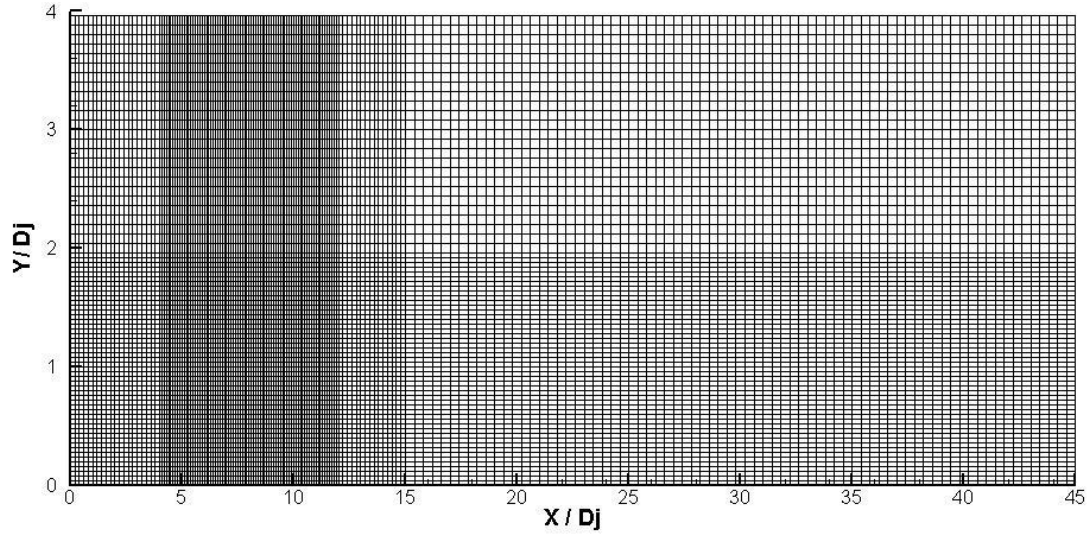

Fig. 2 Mesh used in the RaNS simulation.

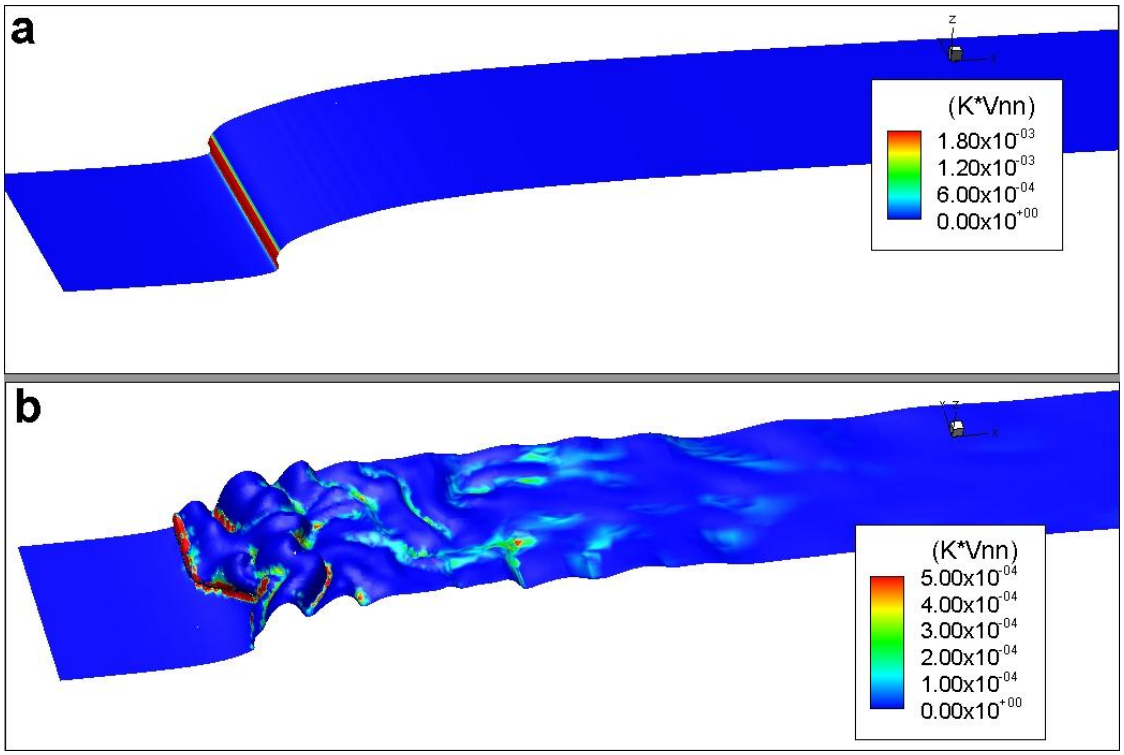

Figure 3: Free surfaces for (a) RaNS and (b) DES simulations, with contours of bubble source intensity, $k\frac{\partial u_n}{\partial n}$

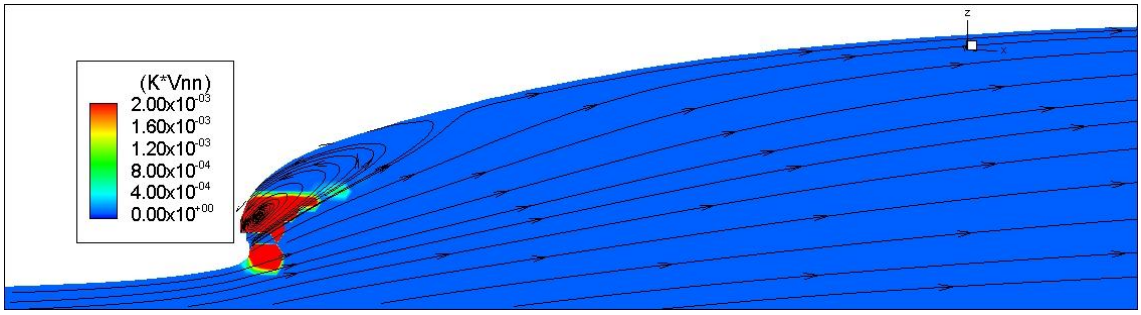

Figure 4: Vortex structure in the roller region predicted by the RaNS simulation.

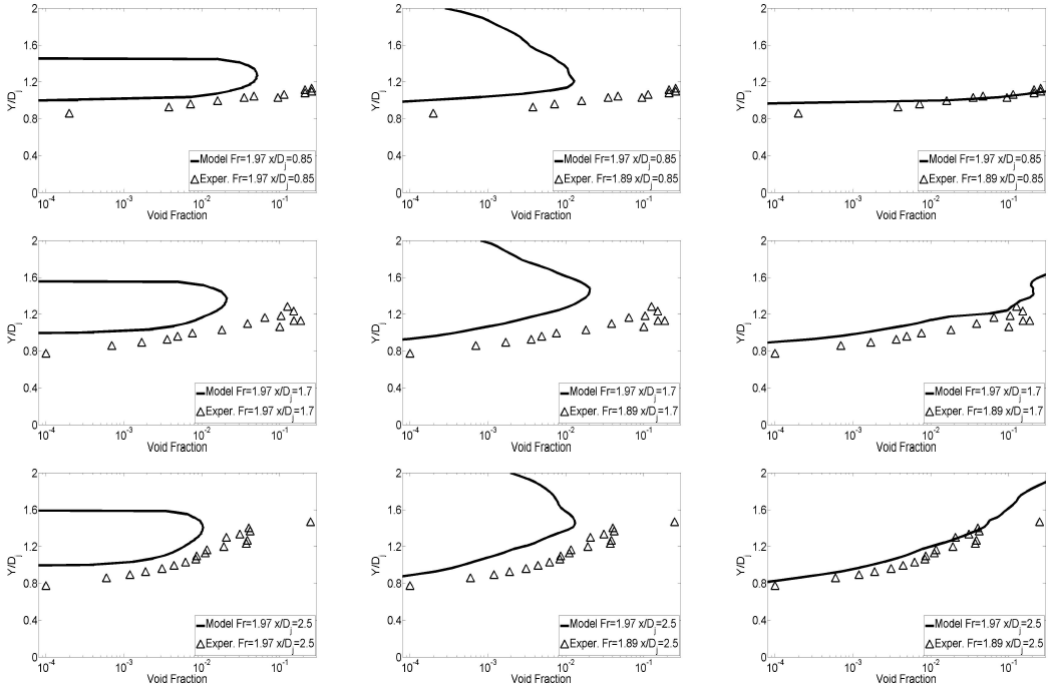

Figure 5: Void fraction distribution predicted by the RaNS (left) and DES (right) two-fluid turbulence models, measured at $X = 0.85D_j, 1.7D_j$ and $2.54D_j$ (from top to bottom). The middle column presents DES results accounting for contributions from bubbles, while excluding those from the wavy interface.